Facile synthesis of Ag/AgVO₃ hybrid nanorods with enhanced electrochemical performance as cathode material for lithium batteries

Shuquan Liang, Jiang Zhou, Anqiang Pan[*], Xuelin Zhang, Yan Tang, Xiaoping Tan, Tao Chen, Ruomei Wu

School of Material Science and Engineering, Central South University, Changsha 410083, PR China

HIGHLIGHTS

► Ag nanoparticles anchored β-AgVO₃ nanorods are prepared by a facile solid-state approach.
► The Ag content in β-AgVO₃/hybrid can be controlled by the calcinations temperature.
► The Ag/β-AgVO₃ hybrid exhibits superior electrochemical performance.
► The superior property is ascribed to the enhanced conductivity and good separation of AgVO₃.

ARTICLE INFO

ABSTRACT

Ag/β-AgVO₃ hybrid nanorods have been successfully prepared by a facile one-step solid-state approach and their electrochemical performance has been evaluated as cathode materials for lithium batteries (LBs). The effects of calcinations temperatures to the morphologies of the material and the content of Ag in the hybrid have been investigated. The Ag/AgVO₃ hybrid synthesized at 420 °C shows well-separated nanorods anchored with Ag nanoparticles. The existence of Ag nanoparticles has been demonstrated to improve the conductivity of the electrode. As a cathode material for lithium batteries, it exhibits high specific capacity, good rate capability and improved cycle stability. Initial specific discharge capacities of 242, 228, 203, 202, 198 mA h g⁻¹ can be achieved at the current densities of 50, 100, 200, 400, 800 mA g⁻¹, respectively. The superior performance is attributed to the combined effect of the electron conductivity improvement by the Ag nanoparticles and the well-separated β-AgVO₃ nanorod structures. The results demonstrate the advantages of the Ag/AgVO₃ hybrid for primary lithium batteries, and the possible application in rechargeable lithium batteries.

1. Introduction

Due to their novel electrical, optical, magnetic and ionic properties, silver vanadium oxides (SVOs) have been extensively investigated and they have found their applications in lithium batteries, gas sensors, catalysts and the advanced biomedical devices et al. [1–6]. Ag₂V₄O₁₁, the most intensively investigated SVOs, have been successfully used in primary lithium batteries for implantable cardioverter defibrillators (ICDs), which stimulates the study on other SVOs. Recently, β-AgVO₃ has attracted much attention because of its superior electrochemical properties. For examples, Zhang et al. [7] have prepared Ag₂V₄O₁₁ nanowires, α-AgVO₃ microrods, and β-AgVO₃ nanowires through a simple hydrothermal route and evaluated their usage in implantable

cardioverter defibrillators (ICDs). Rout et al. [8] have reported the large-scale preparation of β-AgVO₃ nanobelts and an initial discharge capacity of 104 mA h g⁻¹ can be obtained at a field of 0.1 mA cm⁻². Mai et al. [9] have synthesized silver vanadium oxides/polyaniline (SVO/PANI) triaxial nanowires, which exhibit superior electrochemical performance. Although these silver vanadium oxides have attracted extensive attention as cathodes for primary lithium batteries, little work has been focused on their potential usage in rechargeable lithium batteries because of their poor cycling behavior.

Recently, silver nanoparticles have been decorated on other active materials to obtain superior performances, such as chemical stability, high electron conductivity, sensing property, catalytic activity, antibacterial ability and surface-enhanced Raman spectroscopy substrates [10–19]. Dong et al. [12] have developed a one-pot redox route for the synthesis of MoO₃ nanofibers decorated with Ag nanoparticles and reported their improved photocatalytic properties. Wang et al. [14] have fabricated carbon supported Ag

nanoparticles by carbonizing Ag^+/acrylic acid type ion-exchange resin complexes and evaluated their antibacterial properties. Shao et al. [16] have synthesized β-$AgVO_3$ nanoribbons supported Ag nanoparticles via a mechanochemical method using copper and β-$AgVO_3$ as reactants and proposed the surface-enhanced Raman response. Takeuchi et al. [17–19] have reported the Ag^+ in $Ag_2VO_2PO_4$ can be in-situ reduced to metallic silver during discharging, leading to conductivity improvement and resistance decreases in cell, thus high current capability of the material can be achieved. The enhanced performance can be attributed to the good conductivity of the Ag nanoparticles, which results better electron transportation. However, rare work has been reported on the synthesis of silver and silver vanadium oxide composites before cycling. It is expected better electrochemical performance can be obtained because the Ag particles have already been formed on the active material before discharge. However, it is still a big challenge to anchor the silver nanoparticles on the metal oxide with high oxidation state (such as $AgVO_3$ and V_2O_5) because the high valence state of the metal oxides will be reduced during the preparation of Ag nanoparticles.

Herein, a facile one-pot solid-state approach for the large-scale preparation of Ag/β-$AgVO_3$ nanorods hybrid has been developed. The crystal structure and morphologies of as-prepared Ag/$AgVO_3$ hybrid materials are characterized and their electrochemical performances are evaluated. The Ag/$AgVO_3$ hybrid nanorods exhibit high discharge capacity, excellent rate performance and improved cycle stability.

2. Experimental section

All chemicals were of analytical grade and used as received without further purification. V_2O_5 (≥99.0%), $C_2H_2O_4 \cdot 2H_2O$ (≥99.5%) and $AgNO_3$ (≥99.8%) are used as starting materials. Vanadyl oxalic (VOC_2O_4) solution was prepared using a soft chemistry method, which can be found in our earlier work [20–22]. In brief, V_2O_5 (1.2 g) and $C_2H_2O_4 \cdot 2H_2O$ (2.50 g) were added into a beaker containing 40 mL de-ionized water under magnetically stirring at 80 °C until the color of the solution becomes clear blue, which indicates the formation of VOC_2O_4 solution. 20 ml $AgNO_3$ (0.66 M) solution was added into the above VOC_2O_4 under stirring for an hour to make a slurry. Then the slurry was dried overnight in an oven at 80 °C. The as-obtained solid mixture was further calcined in air at various temperatures for 4 h to obtain the final products. The heating ramp rate was set to 5 °C min^{-1}. The Ag/$AgVO_3$ hybrid synthesized at 300 °C, 350 °C, 380 °C, 400 °C, 420 °C and 450 °C are designated as samples A300, A350, A380, A400, A420 and A450, respectively.

A combined Differential Scanning Calorimetry (DSC)/Thermogravimetric Analysis (TGA) instrument (SDT, Q600) was used to study the evolution of the precursor in air at a heating rate of 5 °C min^{-1}. The phase purity and crystallinity of the as-prepared products were studied by X-ray power diffraction (XRD, Rigaku D/max2500 XRD with Cu Kα radiation, λ = 1.54178 Å). The morphologies of the as-prepared products were characterized by scanning electron microscopy (SEM, FEI Sirion200) and transmission electron microscopy (TEM, JEOL JEM-2100F). High-resolution transmission electron microscope (HRTEM) analysis was also performed on the JEOL JEM-2100F transmission electron microscope.

The electrochemical performance measurements were carried out by coin cells (2016 type coin cell). To prepare the cathode, a mixture of the as-prepared Ag/$AgVO_3$ products, acetylene black, and polyvinylidene fluoride (PVDF) binder in a weight ratio of 70:20:10 were dispersed in a N-methyl-2-pyrrolidone (NMP) solution to make a slurry. The slurry was coated on aluminum foil

and dried in a vacuum oven at 100 °C overnight prior to coin-cell assembly. The coin cells were assembled in a glove box (Mbraun, Germany) filled with ultrahigh purity argon using polypropylene membrane as the separator, lithium metal as the anode, and 1 M solution of $LiPF_6$ in ethylene carbonate/dimethyl carbonate (EC/DMC) (1:1 EC:DMC v/v) as the electrolyte. The galvanostatic charge/discharge performances of the electrodes were evaluated at room temperature using an Land Battery Tester (Land CT 2001A, Wuhan, China) within the voltage range of 1.5–3.5 V (vs. Li/Li$^+$) at the current densities of 50, 100, 200, 400 and 800 mA g^{-1}. The loading of the Ag/$AgVO_3$ cathode material for coin cell test is about 1–2 mg.

Cyclic voltammetry (CV) was tested with an electrochemical workstation (CHI660C, China) at a scan rate of 0.5 mV s^{-1} in the voltage range of 1.5–3.5 V (vs. Li/Li$^+$). The electrochemical impedance spectrometry (EIS) was performed on a ZAHNER-IM6ex electrochemical workstation (ZAHNER Co., Germany).

3. Results and discussion

3.1. Structural characterization

Fig. 1 shows the thermal gravimetric analysis (TG) and differential scanning calorimetry (DSC) results of the obtained precursor after drying at 80 °C. The gradual weight loss observed between 50 °C and 230 °C is attributed to the evaporation of the physically absorbed and chemically bonded water of the precursor mixture, which takes a sample weight loss of 7.3%. Then a drastic mass loss on the TG curve and the corresponding exothermal peak on the DSC curve at 248 °C were observed. The exothermal peak is related to the thermal co-decomposition of the precursor made of the VOC_2O_4 and $AgNO_3$. The second small exothermal peak at 330 °C is attributed to the further oxidation of V^{4+} to V^{5+} in air. A sharp endothermic peak of the DSC curve at 461 °C may be the melting point of $AgVO_3$.

The XRD patterns for the Ag/$AgVO_3$ materials synthesized at different temperatures are shown in Fig. 2. As indexed in Fig. 2, the (111), (200) and (220) faces are well detected, which can be ascribed to face-centered cubic Ag phase [space group: $Fm\bar{3}m$ (225), JCPDS card 04-0783], and the (−311) diffraction peak can be indexed to the V_2O_5 phase [space group: $C2/c$ (15), JCPDS card 54-0513]. Also the formation of $AgVO_3$ could be clearly identified. The intensity of (111), (200), (220) and (−311) diffraction peaks become weaker at 380 °C, indicating the depletion of Ag phase and
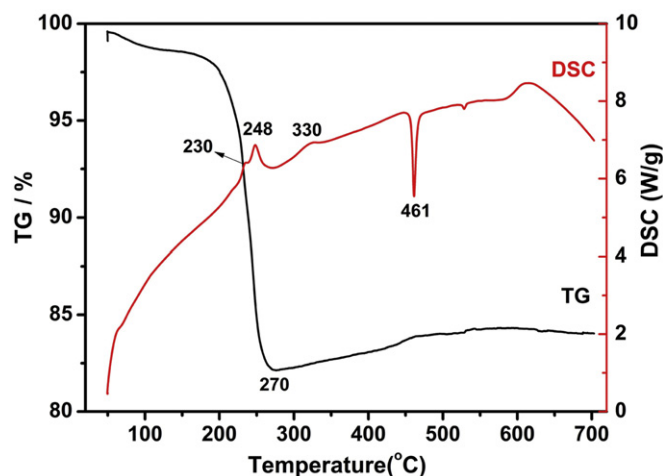

Fig. 1. TG and DSC results for the precursor after drying at 80 °C. The temperature ramp rate was set to 5 °C min^{-1}.

V_2O_5 phase to form $AgVO_3$ phase. Further increasing the calcinations temperature to 400 °C, the (−311) diffraction peak disappears, which indicates the hybrid materials are mainly consisted of $AgVO_3$ and Ag phase. All the diffraction peaks can be readily indexed to the β-$AgVO_3$ phase [space group: $I2/m$ (12), JCPDS card 29-1154] at 450 °C. No other phases are detected, which indicates the high purity of the product. This result is corresponding well with the gradual weight increase from 270 °C to 461 °C shown on the TG curve (Fig. 1). V_2O_5 and Ag can react in air to form $AgVO_3$ and the reaction can be expressed as follows:

$$2V_2O_5 + 4Ag + O_2 \rightarrow 4AgVO_3 \tag{1}$$
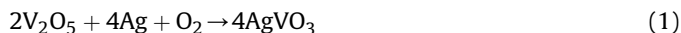
The XRD results indicate the content of metallic Ag phase reduces in the Ag/$AgVO_3$ hybrid materials with the increasing of calcinations temperatures.

Fig. 3 shows the SEM images of the products prepared at different temperatures and different time. The calcinations temperature and sustaining time are demonstrated to have a big effect to the products' final morphologies. As is showed in Fig. 3a, the particles of the product are irregular, which are typically composed of nanoparticles and nanorods. The particles with ample space between each other can be observed, much like a big stone splitting into innumerable small particles. Raising the calcinations temperature to 400 °C (Fig. 3b), most of the obtained particles become rods with the diameter ranging from dozens of nanometers to several hundred nanometers, as well as some small particles about 100 nm. When the calcinations temperature was raised to 420 °C for 4 h (Fig. 3d), the product is composed of a large quantity of one-dimensional nanorods and becomes more homogeneously separated with less agglomeration. The nanorods with smooth surface are very uniform and the diameters of which are ranging from 100 nm to 1 μm, and the length of which can be several micrometers. Further increasing the calcination temperature to 450 °C, the particles are of micro-rod shape, the diameter of which is between 1 and 3 μm. Fig. 3c–e shows the morphologies of the products prepared at 420 °C for different hours (2 h, 4 h and 8 h, respectively). As shown in Fig. 3c, the diameters of the particles are in a wide range from 100 nm to 2 μm, but with limited aggregation. The particles are much larger and more densely packed for 8 h prepared samples. It is believed the evolution of the morphologies is controlled by the kinetics of the phase transition. The

spontaneous growth of small particles at high temperatures and long reaction time may be ascribed to the formation of larger particles, which are more kinetically favorable to reduce the surface energy [20]. Fig. 3g shows the SEM image of the annealed product prepared at 420 °C for 4 h at high magnification. Nanoparticles are clearly observed on the surface of the rods. The element composition of the selected area (marked in Fig. 3g) is studied by EDX and the result is shown in Fig. 3h. Ag, V, and O elements are well detected and the content of Ag and V elements are 26.54% and 21.98%, respectively. The Ag:V molar ratio is greater than the stoichiometric ratio of 1:1, which suggests the nanoparticles are silver particles.

To further confirm the structure of the Ag/AgVO3 hybrid, TEM and HRTEM are employed to characterize the structures. Fig. 4a shows the TEM image of Ag/$AgVO_3$ nanorods prepared at 420 °C for 4 h and the inset HRTEM of the Ag/$AgVO_3$ nanorods and the corresponding FFT pattern. As indicated in the HRTEM (the inset of Fig. 4a), the lattice spacing of 2.05 Å corresponds to the plane distance of the (710) face of β-$AgVO_3$. This can be reflected by the fast Fourier transform (FFT) pattern. The nanoparticles anchored on the surfaces of β-$AgVO_3$ nanorods with the diameter around 25 nm are clearly observed. The result corresponds well with the SEM image shown in Fig. 3g. Fig. 4b shows the HRTEM image of a single silver nanoparticle on surface of the rod as indicated by the red square in Fig. 4a. The lattice spacing is 2.38 Å, which corresponds well to the lattice spacing of (111) planes for cubic Ag phase. It is also reflected in the corresponding fast Fourier transform (FFT) pattern (inset Fig. 4b). The results indicate the Ag nanoparticles anchored on β-$AgVO_3$ nanorods would be beneficial to obtain better electrochemical performance because of the improved conductivity.

3.2. Electrochemical performance

Fig. 5a shows the first discharge curves of the as-prepared Ag/$AgVO_3$ hybrid materials fabricated at different temperatures at the current density of 50 mA g^{-1}. The discharge plateaus of A380 electrode are quite different from the other electrodes, which can be attributed to the impurity of the product. As evidenced by XRD pattern of A380 product, the V_2O_5 impurity phase can be clearly observed, which would influence the discharge curve of pure $AgVO_3$ electrode. However, the discharge curves of A400, A420, and A450 are consistent with the typical curves of lithium-ion intercalation in $AgVO_3$ crystalline structures [7,9]. The specific discharge capacities rank in the following order: A420 > A400 > A380 > A450. It can be seen that A420 electrode exhibits the highest specific capacity of 242 mA h g^{-1}, while the A450 electrode delivers a lower discharge capacity of 212 mA h g^{-1}.

The typical electrochemical impedance spectra of the electrodes made from the as-prepared Ag/$AgVO_3$ hybrid materials are performed and the Nyquist plots are shown in Fig. 5b. It can be observed that all the impedance spectra of these electrodes have a similar shape that each plot has a semicircle in the high-frequency region and a straight line in the low-frequency region. The semicircle can be associated with the passivating film formed on the material and the charge-transfer process [7,23], and the straight line is related to the lithium diffusion in the electrode material [9,24,25]. The inset is the equivalent circuit model for the impedance spectra. R_s is the combination of electrolyte resistance and ohmic resistances of cell components. R_f and R_{ct} are the film resistance and charge-transfer resistance, respectively. CPE$_1$, CPE$_2$, and Z_W are the film capacitance, double layer capacitance, and the Warburg impedance, respectively. Table 1 shows the primary simulation parameters of the as-prepared Ag/$AgVO_3$ hybrid materials. As can be clearly seen in the table, the R_{ct} values of the hybrid
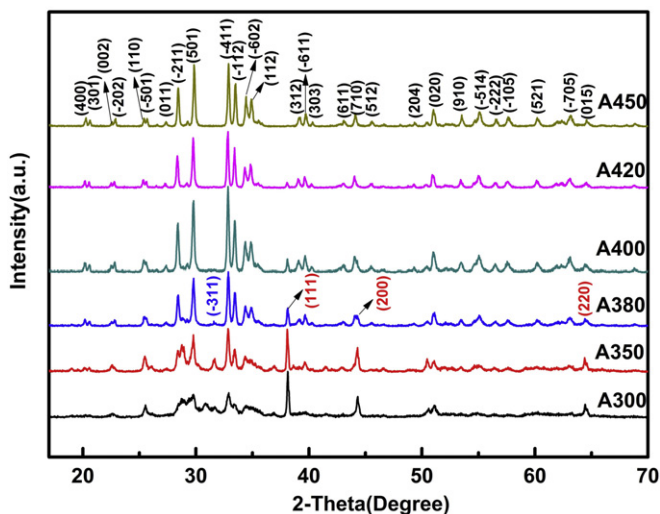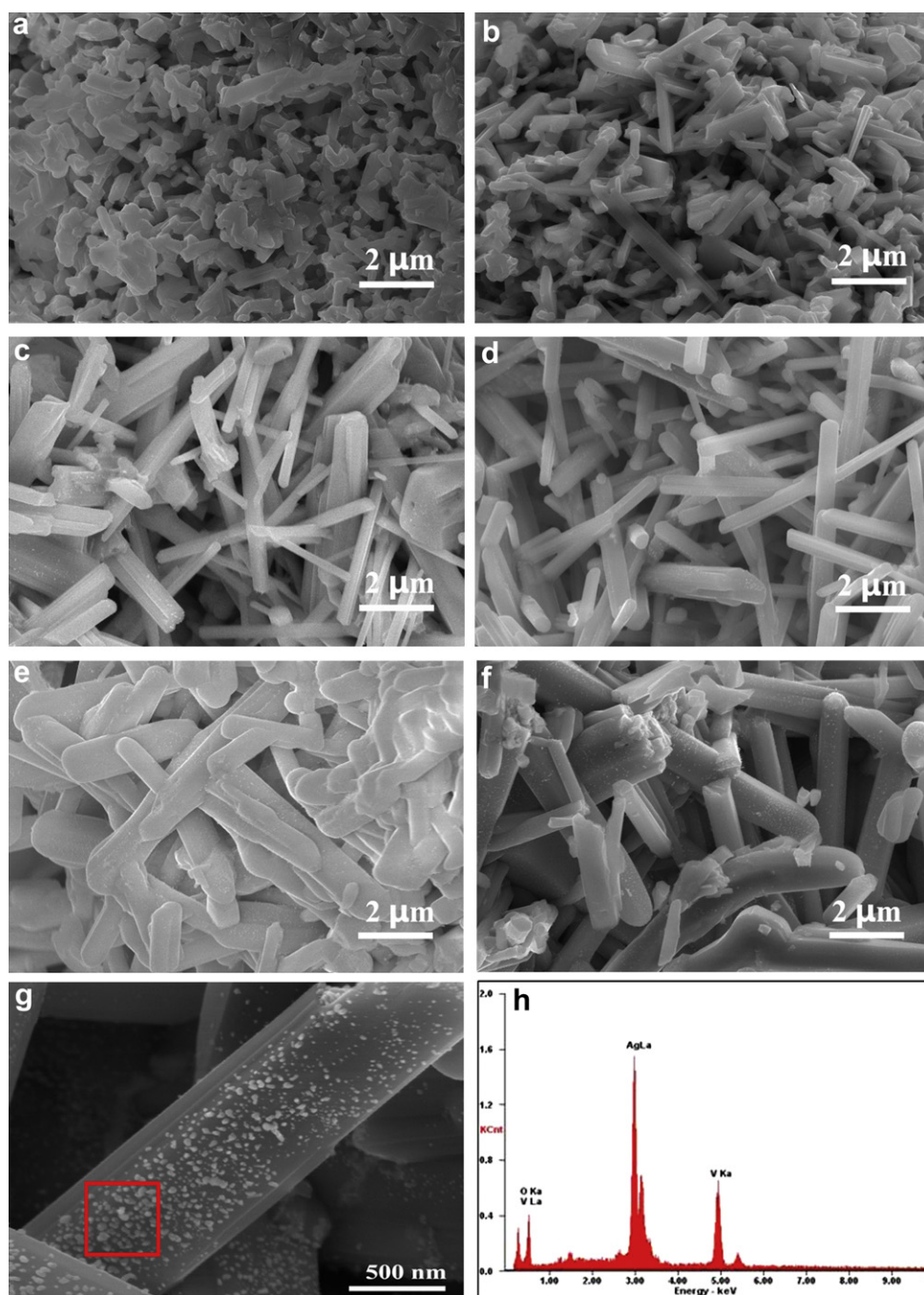

Fig. 2. XRD patterns of the Ag/$AgVO_3$ hybrid synthesized at different temperatures (300 °C, 350 °C, 380 °C, 400 °C, 420 °C and 450 °C) for 4 h, which are designated as samples A300, A350, A380, A400, A420 and A450, respectively.

Fig. 3. SEM images of the Ag/AgVO₃ hybrid materials synthesized at different temperature for different period of time: (a) 380 °C, 4 h; (b) 400 °C, 4 h; (c) 420 °C, 2 h; (d) 420 °C, 4 h; (e) 420 °C, 8 h; (f) 450 °C, 4 h; (g) High magnification SEM image of the product prepared at 420 °C for 4 h; (h) The EDX pattern of the area marked in g.

materials increased with the calcination temperatures, which indicate the percentage of Ag nanoparticles has great effect on the charge-transfer resistance. Moreover, these values are much smaller than those for pure β-AgVO₃, and the silver vanadium oxides/polyaniline triaxial nanowires previously reported [9]. Such a small charge-transfer resistance may be ascribed to the Ag nanoparticles, which provides high electronic conductivity for the material and thus results in faster electron transportation. There should be an optimized content of Ag nanoparticles in the Ag/β-AgVO₃ hybrid to achieve the best performance because of its inactive to the lithium ions intercalation, although higher Ag content can improve the conductivity of the hybrid nanorods. As

shown in Fig. 5a, the A420 electrode has the highest capacity than the others. This can be attributed to the combined effect of the conductivity and morphologies of the β-AgVO₃. The presence of Ag nanoparticles can increase the electronic conductivity but it has no contribution to capacity of the active material, thus the more content of metallic silver phase, the lower theoretical capacity of the material will be. Secondly, the particle size and morphologies also can affect the electrochemical performance. Comparing to the larger particles, the smaller particles with ample space between each other are beneficial to the faster diffusion of Li⁺ ions and the easier penetration of the electrolyte, and higher capacity can be achieved [26,27].
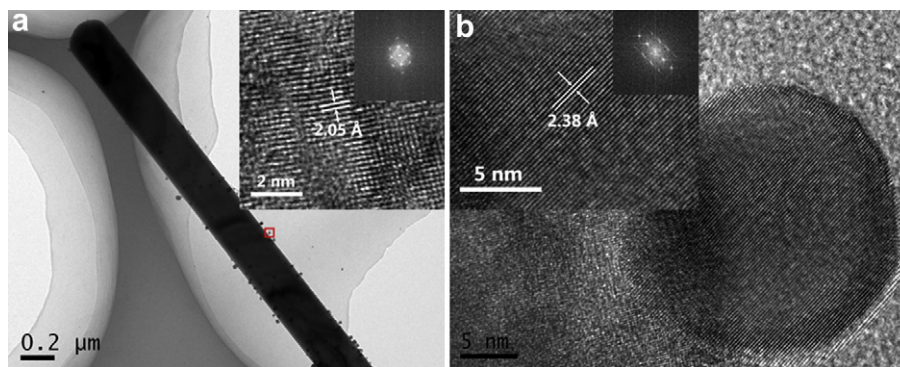
Fig. 4. (a) TEM image of an individual Ag/AgVO₃ nanorod synthesized at 420 °C for 4 h. The inset shows the HRTEM of the Ag/AgVO₃ nanorod and the corresponding FFT pattern. (b) HRTEM image of a single Ag nanoparticle marked in Fig. 4a, inset shows the corresponding FFT pattern.

Fig. 6a shows the first five successive CV curves of the A420 hybrid material at a scan rate of 0.5 mV s^{-1}. Three strong cathodic peaks located at 2.7, 2.18 and 2.0 V vs. Li/Li$^+$, and one anodic peak at 2.89 V vs. Li/Li$^+$ are clearly detected, which corresponds to the Li$^+$ ions insertion/extraction reactions. All the cathodic peaks are associated with the reduction of Ag$^+$ to Ag^0 that deposited as metallic silver; the cathodic peaks located at 2.18 and 2.0 V can

mainly attributed to the reduction of V^{5+} to V^{4+} and partial reduction of V^{4+} to V^{3+}, respectively [7]. The anodic peak located at 2.89 V may be resulted from the oxidation of V^{4+} to V^{5+} and V^{3+} to V^{4+}. The peaks decreases significantly after the first cycle, and the cathodic peaks shift to 2.33 and 1.79 V vs. Li/Li$^+$, but the anodic peak do not change much. The cyclic voltammograms are quite similar for the later cycles, which indicate the improved cycle stability.

In order to investigate the structural changes after cycling, the ex-situ XRD patterns of the electrodes before electrochemical measurement, after first cycle and fifth cycle are shown in Fig. 6b. The strongest diffraction peaks observed at $2\theta = 65.133°$, 78.227° can be ascribed to centered cubic Al phase (JCPDS Card No.04-0787), which was used as the current collector. The XRD peaks of Ag/AgVO₃ hybrid can be clearly identified before cycling. After first cycle, the peaks assigned to AgVO₃ phase has disappeared and do not show again upon cycling (shown in Fig. 6b). The result indicates the irreversible phase transformation and the formation of amorphous phase after the initial cycle, which explain the serious capacity loss in the first cycle. And no new phase change happens upon cycling, suggesting the improved cycling behavior. Furthermore, the relative intensity of the diffraction peaks observed at $2\theta = 38°$, 44°, 64° and 77°, corresponding to the (111), (200), (220), (311) planes of the centered cubic Ag phase are getting stronger. This result confirms the reduction of Ag$^+$ to metallic silver upon cycling as discussed above.

Fig. 7a shows the initial discharge curves of the A420 electrodes at different current densities. Three distinct plateaus are exhibited at the current densities of 50 mA g^{-1} and 100 mA g^{-1}, which are in good agreement with the CV results (shown in Fig. 6a). The A420 electrode exhibits the specific discharge capacities of 228, 204, 202, 198 mA h g^{-1} at the current densities of 100, 200 400, and 800 mA g^{-1}, respectively. These electrochemical results demonstrate the Ag/AgVO₃ hybrid nanorods have excellent rate capability, which is raised from the enhanced electron conductivity by the anchored Ag nanoparticles.

As is known to us, the well-established irreversible silver displacement reaction of the silver vanadium oxides (SVOs) have
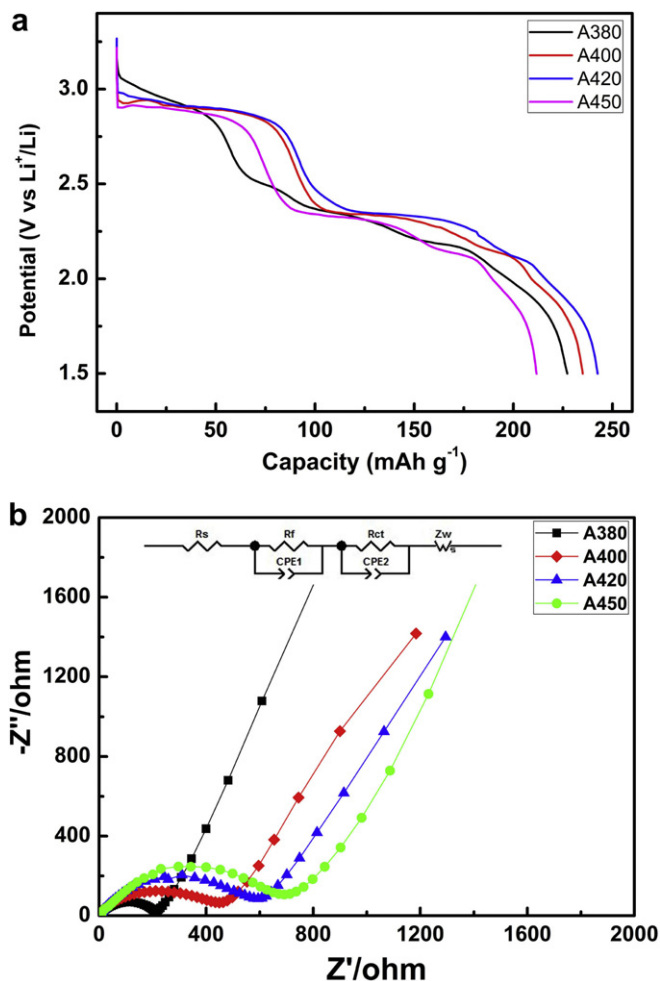
Fig. 5. (a) first discharge curves of the Ag/AgVO₃ hybrid materials synthesized at different temperatures. (b) Nyquist plot of the Ag/AgVO₃ hybrid materials synthesized at different temperatures for 4 h.

Table 1
The EIS simulation parameters of Ag/AgVO₃ hybrid materials.

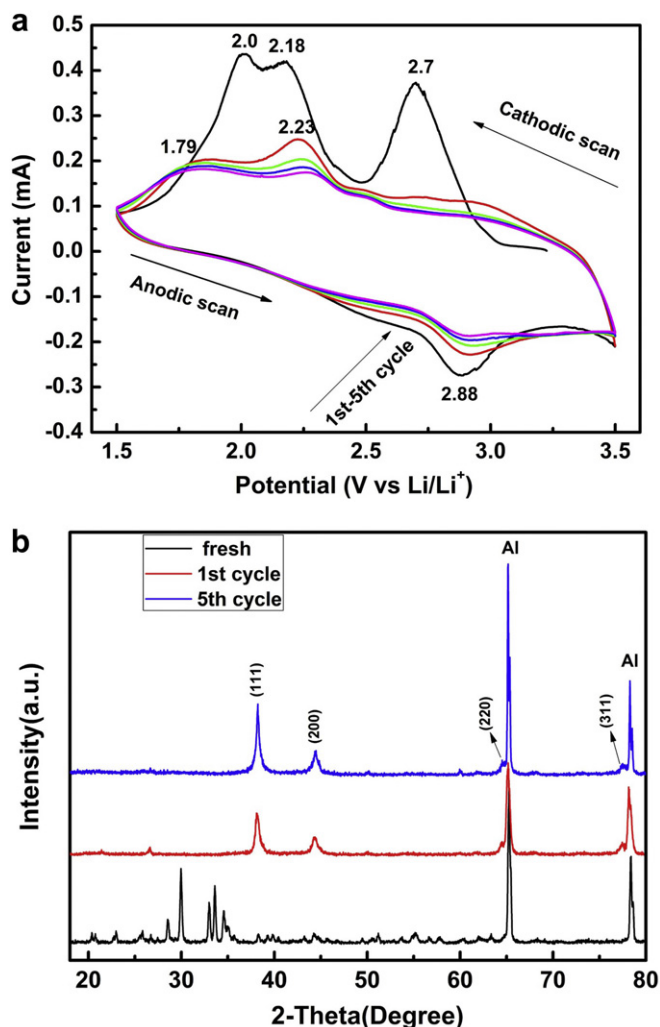| Samples	R_s (Ω)	R_f (Ω)	R_{ct} (Ω)
A380	1.442	28.83	131.9
A400	1.539	57.77	265.9
A420	5.186	59.53	404.5
A450	6.046	56.21	488.6

Fig. 6. (a) the first five CV curves of the A420 electrodes; (b) Ex-situ XRD patterns of the A420 electrodes: Fresh, after first cycle and after fifth cycle.
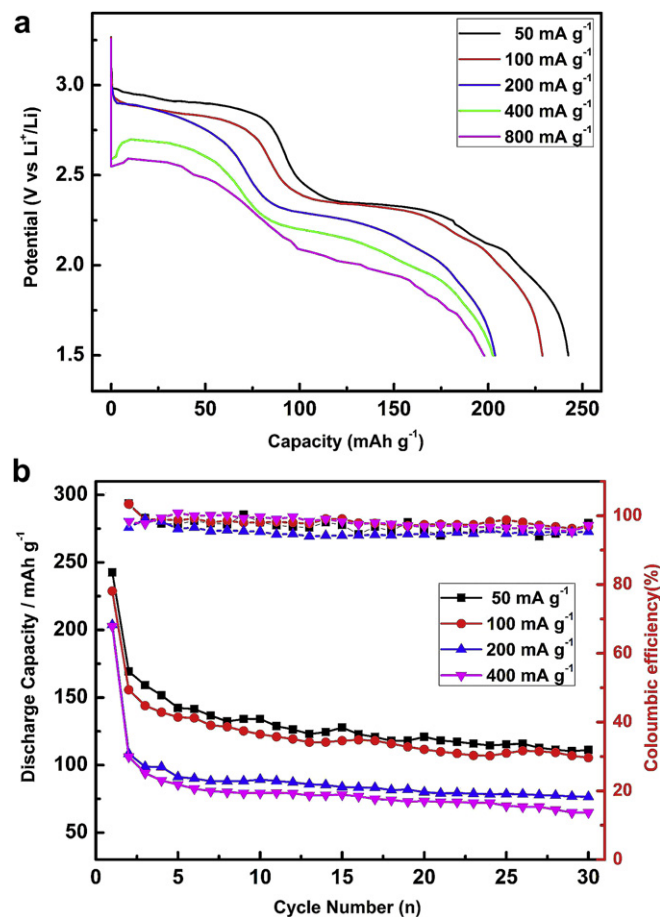

Fig. 7. (a) first discharge curves of the A420 electrodes at different current densities; (b) Cycling performances of the A420 electrodes at different current densities.

generally investigated as cathode materials for implantable cardioverter defibrillators (ICDs) and their cycling performances have been rarely reported. In this work, we have evaluated the A420 electrodes at different current densities and the results are showing in Fig. 7b. A large initial discharge capacity loss is clearly observed at different current densities, which is ascribed to the irreversible structure transformation as indicated by the CV and ex-situ XRD result. The capacity loss upon cycling becomes gentle after the first cycle. The electrode retains a specific discharge capacity of 111 mA h g^{-1} after 30 cycles at the current density of 50 mA g^{-1}, with a fading rate of 1.49% per cycle based on the second cycle's discharge capacity. The specific discharge capacities of 30th cycles are 106, 77 and 65 mA h g^{-1} at the current densities of 100, 200 and 400 mA g^{-1}, respectively with the coulombic efficiency above 95% (Fig. 7b) at different current densities.

Table 2 lists the electrochemical performance of previous reported silver vanadium oxides (SVOs) and our results. As shown in Table 2, our Ag/AgVO$_3$ hybrid electrodes have very good rate capability and cycle stability. The initial capacity is only second to the hydrothermal prepared samples [7,28], but possess much improved cycle stability. For example, the β-AgVO$_3$ prepared by hydrothermal process have an initial specific discharge capacity of 302 mA h g^{-1}, but only maintains 30% of the initial capacities after 20 cycles. The β-AgVO$_3$ prepared by a hydrothermal method [8] and sono-chemical route [29] show a very low initial capacities of

104 mA h g^{-1} and 102 mA h g^{-1}, respectively. The Ag$_2$V$_4$O$_{11}$ material prepared by hydrothermal method also suffers terrible cycle stability, although a high initial capacity can be obtained. Chen et al. [28] obtained the Ag$_2$V$_4$O$_{11}$/Ag nanobelts with a high capacity of 276 mA h g^{-1}, but only about 10.9% of the initial capacity can be retained after 20 cycles at even much lower current density of 20 mA g^{-1}. Recently, Mai et al. [9] have prepared the silver vanadium oxides/polyaniline (SVO/PANI) tri-axial nanowires with enhanced electrochemical properties by combining the *in situ* chemical oxidative polymerization and the interfacial redox reaction. The SVO/PANI triaxial nanowire demonstrated a higher initial capacity and the better cycle stability than the pure β-AgVO$_3$ nanowires. However, the existence of the PANI would decrease the specific initial capacity of the SVO/PANI triaxial nanowire because of its much lower capability to accommodate lithium ions. The Ag/AgVO$_3$ hybrid nanorods in this work not only exhibit a relatively high initial specific discharge capacity of 242 mA h g^{-1} at a current density of 50 mA g^{-1}, but also show the better cycle stability. The superior electrochemical performances including excellent rate performance and good cycle stability of the as-prepared product can be attributed to the Ag nanoparticles decorated on the well-separated β-AgVO$_3$ nanorods. The metallic silver nanoparticles attached on the surfaces of the nanorods can increase the electronic conductivity of the β-AgVO$_3$ nanorods. The nano-sized β-AgVO$_3$ rod could decrease the lithium-ion diffusion and the electron transportation distance [20,27]. The ample space between each rod would allow easy penetration of electrolyte, thus improves the wettability of the electrode [21]. The electrochemical performance

Table 2
Electrochemical properties of SVOs prepared by different methods.

Synthesis method (ref)	Composition	Current density	Capacity (mA h g^{-1}) (cycle number)	Capacity retention
Base on AgVO$_3$ nanowires [9]	AgVO$_3$/PANI	30 mA g^{-1} (211)	211(1)—131 (20)	62%
Hydrothermal [7]	β-AgVO$_3$	0.01 mA (302.1) 0.1 mA (272.7)	302.1(1) −90.6(20)	30%
Hydrothermal [8]	β-AgVO$_3$	0.1 mA cm^{-2} (104)	–	–
Sonochemical route [26]	β-AgVO$_3$	125 mA g^{-1} (102)	–	–
Hydrothermal [25]	Ag/Ag$_2$V$_4$O$_{11}$	20 mA g^{-1} (276) 100 mA g^{-1} (150)	276(1)—30 (20)	10.9%
This work	Ag/AgVO$_3$	50 mA g^{-1} (242.5) 100 mA g^{-1} (228.8) 200 mA g^{-1} (203.7) 400 mA g^{-1} (202.7) 800 mA g^{-1} (198)	242.5(1)—111(30)	46%

demonstrates that the as-prepared Ag/AgVO$_3$ hybrid nanorods are a promising cathode material in the field of primary Li-SVO batteries for ICDs. It also can be potential cathode materials for rechargeable lithium-ion batteries (LIBs).

4. Conclusion

In summary, Ag/AgVO$_3$ hybrid materials with enhanced electrochemical properties have been successfully prepared by a one-step solid-state approach. The calcination temperatures have great effect to the morphologies of the Ag/β-AgVO$_3$ and the content of Ag nanoparticles in the hybrid. The Ag/AgVO$_3$ hybrid material synthesized at 420 °C for 4 h with the smooth surface are very uniform and well-separated. The electrochemical performance of the as-prepared Ag/AgVO$_3$ hybrid demonstrates high discharge capacity, excellent rate performance and good cycle stability. This superior electrochemical performance is attributed to the anchored Ag nanoparticles that increase the electronic conductivity and the well-separated nanorods that favor the Li$^+$ ion diffusion and electrolyte penetration. The good performances suggest they may be potential cathode materials for primary lithium batteries or rechargeable lithium-ion batteries (LIBs).

References

[1] K.J. Takeuchi, A.C. Marschilok, S.M. Davis, R.A. Leising, E.S. Takeuchi, Coord. Chem. Rev. 283 (2001) 219—221.
[2] L.Q. Mai, L. Xu, Q. Gao, C.H. Han, B. Hu, Y.Q. Pi, Nano Lett. 10 (2010) 2604—2608.
[3] C.J. Mao, X.C. Wu, H.C. Pan, J.J. Zhu, H.Y. Chen, Nanotechnology 16 (2005) 2892—2896.
[4] K. West, A.M. Crespi, J. Power Sources 54 (1995) 334—337.
[5] J. Xu, C.G. Hu, Y. Xi, B.Y. Wan, C.L. Zhang, Y. Zhang, Solid State Sci. 14 (2012) 535—539.
[6] M.I. Bertoni, N.J. Kidner, T.O. Mason, T.A. Albrecht, E.M. Sorensen, K.R. Poeppelmeier, J. Electroceram. 18 (2007) 189—195.
[7] S.Y. Zhang, W.Y. Li, C.S. Li, J. Chen, J. Phys. Chem. B 110 (2006) 24855—24863.
[8] C.S. Rout, U.K. Gautam, Y.S. Bando, D. Rangappa, X.S. Fang, L. Li, D. Golberg, Sci. Adv. Mater. 2 (2010) 407—412.
[9] L.Q. Mai, X. Xu, C.H. Han, Y.Z. Luo, L. Xu, Y.A. Wu, Y.L. Zhao, Nano Lett. 11 (2011) 4992—4996.
[10] C.L. Lu, Q.M. Shen, X.M. Zhao, J.J. Zhu, X.F. Guo, W.H. Hou, Sens. Actuators. B 150 (2010) 200—205.
[11] U. Schlecht, B. Guse, I. Raible, T. Vossmeyer, M. Burghard, Chem. Commun. (2004) 2184—2185.
[12] W.J. Dong, Z. Shi, J.J. Ma, C.M. Hou, Q. Wan, S.H. Feng, A. Cogbill, Z.R. Tian, J. Phys. Chem. B 110 (2006) 5845—5848.
[13] R.D. Holtz, A.G. Souza Filho, M. Brocchi, D. Martins, N. Durán, O.L. Alves, Nanotechnology 21 (2010) 185102.
[14] B.L. Wang, C.G. Tian, C.Y. Zheng, L. Wang, H.G. Fu, Nanotechnology 20 (2009) 025603.
[15] R.D. Holtz, B.A. Lima, A.G. Souza Filho, M. Brocchi, O.L. Alves, Nanomed. Nanotechnol. Biol. Med. (2012). http://dx.doi.org/10.1016/j.nano.2011.11.012.
[16] M.W. Shao, L. Lu, H. Wang, S. Wang, M.L. Zhang, D.D.D. Ma, S.T. Lee, Chem. Commun. (2008) 2310—2312.
[17] A.C. Marschilok, K.J. Takeuchi, E.S. Takeuchi, Electrochem. Solid-State Lett. 12 (2009) A5—A9.
[18] E.S. Takeuchi, A.C. Marschilok, K. Tanzil, E.S. Kozarsky, S. Zhu, K.J. Takeuchi, Chem. Mater. 21 (2009) 4934—4939.
[19] A.C. Marschilok, E.S. Kozarsky, K. Tanzil, S. Zhu, K.J. Takeuchi, E.S. Takeuchi, J. Power Sources 195 (2010) 6839—6846.
[20] A.Q. Pan, J.G. Zhang, Z.M. Nie, G.Z. Cao, B.W. Arey, G.S. Li, S.Q. Liang, J. Liu, J. Mater. Chem. 20 (2010) 9193—9199.
[21] A.Q. Pan, J. Liu, J.G. Zhang, G.Z. Cao, W. Xu, Z.M. Nie, X. Jie, D. Choi, B.W. Arey, C.M. Wang, S.Q. Liang, J. Mater. Chem. 21 (2011) 1153—1161.
[22] A.Q. Pan, J.G. Zhang, G.Z. Cao, S.Q. Liang, C.M. Wang, Z.M. Nie, B.W. Arey, W. Xu, D.W. Liu, J. Jie, G.S. Li, J. Liu, J. Mater. Chem. 21 (2011) 10077—10084.
[23] C. Li, W. Wei, S. Fang, H. Wang, Y. Zhang, Y. Gui, R. Chen, J. Power Sources 195 (2010) 2939—2944.
[24] J.W. Lee, B.N. Popov, J. Power Sources 161 (2006) 565—572.
[25] R.P. Ramasamy, C. Feger, T. Strange, B.N. Popov, J. Appl. Electrochem. 36 (2006) 487—497.
[26] P.G. Bruce, B. Scrosati, J.M. Tarascon, Angew. Chem. Int. Ed. 47 (2008) 2930—2946.
[27] N. Sivakumar, S.R.P. Gnanakan, K. Karthikeyan, S. Amaresh, W.S. Yoon, G.J. Park, Y.S. Lee, J. Alloys Compd. 509 (2011) 7038—7041.
[28] Z.J. Chen, S.K. Gao, R.H. Li, M.D. Wei, K.M. Wei, H.S. Zhou, Electrochim. Acta 53 (2008) 8134—8137.
[29] C.J. Mao, X.C. Wu, J.J. Zhu, J. Nanosci. Nanotechnol. 8 (2008) 3203—3207.